energy&fuels

ARTICLE

pubs.acs.org/EF

Gas Production from Hydrate-Bearing Sediments: The Role of Fine Particles

J. W. Jung,*[,†] J. Jang,[§] J. C. Santamarina,[†] C. Tsouris,[‡] T. J. Phelps,[‡] and C. J. Rawn[‡]

[†]School of Civil and Environmental Engineering, Georgia Institute of Technology, Georgia 30332, United States

[§]Department of Civil and Environmental Engineering, Wayne State University, Michigan 48202, United States

[‡]Oak Ridge National Laboratory, P.O. Box 2008, Oak Ridge, Tennessee 37831-6181, United States

ABSTRACT: Even a small fraction of fine particles can have a significant effect on gas production from hydrate-bearing sediments and sediment stability. Experiments were conducted to investigate the role of fine particles on gas production using a soil chamber that allows for the application of an effective stress to the sediment. This chamber was instrumented to monitor shear-wave velocity, temperature, pressure, and volume change during CO_2 hydrate formation and gas production. The instrumented chamber was placed inside the Oak Ridge National Laboratory Seafloor Process Simulator (SPS), which was used to control the fluid pressure and temperature. Experiments were conducted with different sediment types and pressure−temperature histories. Fines migrated within the sediment in the direction of fluid flow. A vuggy structure formed in the sand; these small cavities or vuggs were precursors to the development of gas-driven fractures during depressurization under a constant effective stress boundary condition. We define the critical fines fraction as the clay-to-sand mass ratio when clays fill the pore space in the sand. Fines migration, clogging, vugs, and gas-driven fracture formation developed even when the fines content was significantly lower than the critical fines fraction. These results show the importance of fines in gas production from hydrate-bearing sediments, even when the fines content is relatively low.

1. INTRODUCTION

Gas production from hydrate-bearing sediments is expected to cause fluid volume expansion, gas and water flow, temperature decrease due to both depressurization and endothermic hydrate dissociation, ice and secondary hydrate formation, softening of the sediment skeleton, and changes in porosity and effective stress. Other phenomena may develop as well, including fines migration and pore clogging,[1−3] sand production,[4] grain crushing,[5−7] and gas-driven fractures in sediments.[8] These emergent processes may cause sediment instability, formation clogging, sand production, bore-hole failure, retardation of gas production, and low gas recovery efficiency.

Several analytical and numerical models have been developed to analyze gas production from hydrate-bearing sediments.[9−14] These models capture thermodynamic conditions and standard macro-scale mechanical behavior of hydrate-bearing sediments, but have not yet considered phenomena such as fines migration and its implications.

Small-scale laboratory experiments with homogeneous internal and boundary conditions have focused on the effect of pressure, temperature, and inhibitors on gas production rate and the cumulative amount of produced gas.[15−20] Larger scale laboratory experiments are needed to reproduce and capture spatially and temporally varying processes in gas production from hydrate-bearing sediments, such as the potential development of localization/bifurcation processes that may emerge in relation to fines migration. Yet, large-scale testing is particularly challenging in the study of hydrate-bearing sediments because of the high pressure needed to attain stability conditions, the need for concurrent effective stress control, and ensuing safety considerations. In this study, we used the large-size Seafloor Process Simulator (SPS) at the Oak Ridge National Laboratory to house an effective stress cell.[21]

2. EXPERIMENTAL STUDY

2.1. Devices. *Seafloor Process Simulator (SPS).* This 72-L vessel was constructed from corrosion-resistant Hastelloy (Figure 1a). The simulator has a maximum 21 MPa working pressure, and 41 ports for instrumentation. It was housed inside of a cold room with a working temperature range from −2 to 20 °C.

Effective Stress Cell. An effective stress cell of sample size 300 mm high and 154 mm diameter was placed inside the SPS (Figure 1b). The fixed bottom plate had a fluid injection port. The perforated top plate allowed for free-gas and water flow and could move up and down to follow the sediment volume change. A spring (k = 306 N/cm) on the top plate was used to apply a predetermined effective stress on the sediment while maintaining zero lateral-strain conditions. In this study, a nominal vertical effective stress σ_v' = 100 kPa was applied to the sediment in Tests 2, 3, and 4 (Note: friction along the walls reduces the vertical effective stress toward the bottom of the cell; the exponential stress reduction predicts a bottom vertical stress as low as 40 kPa). The effective stress σ_v' = 100 kPa (∼10 m depth) was selected to allow for proper V_s measurements and sediment expansion/subsidence under a stiffness-controlled boundary condition within space restrictions in the SPS. These experimental conditions are analyzable and can be analytically extended to hydrate-bearing sediments in nature.

Instrumentation. The sediment vertical displacement during hydrate formation and gas production was measured using a Linear Variable Differential Transformer (LVDT) that rested on the top plate of the effective stress cell (Figure 1b). Sensors were located at preselected positions attached onto a frame buried in the sediment. There were three pairs of bender elements (Figure 1b): the source bender elements in each pair were connected to a signal generator, which sent a step

Received: December 6, 2010
Revised: November 16, 2011
Published: November 16, 2011

function signal every 20 ms; the receiver bender elements were connected to a preamplifier and a digital storage oscilloscope. Three thermocouples were buried in the sediment at the same heights as the three pairs of bender elements, and a fourth thermocouple was used to measure the temperature on top of the sediment. Thermocouple 5 was located inside the fluid injection port of the effective stress cell, and thermocouple 6 was placed inside the SPS to measure the gas temperature. A pressure transducer provided gas pressure measurements inside the SPS, and a second pressure transducer was connected to the fluid injection port at the bottom plate of the effective stress cell to monitor bottom fluid pressure. A data logger was used to record all pressures, temperatures, and the vertical displacement every four seconds.

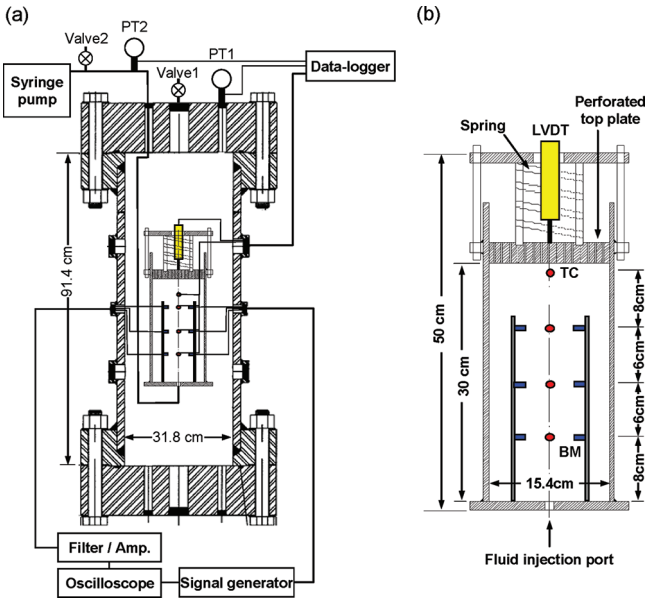

Figure 1. Devices and instrumentation. (a) Seafloor Process Simulator and peripheral electronics. (b) Effective stress cell instrumented with linear variable differential transformer (LVDT) for sediment displacement measurements, bender element (BM) for shear-wave velocity measurements, and thermocouples (TC) for temperature measurements.

Sediments. The first two tests (Tests 1 and 2) involved clean Ottawa 20/30 sand (US Silica, passing U.S. standard #20 sieve of size 850 μm, and retained on #30 sieve of size 600 μm), which was placed in the soil chamber with an initial porosity of $n = 0.4$. A mixture of Ottawa 80/140 sand (US Silica, passing U.S. standard #80 sieve of size 180 μm, and retained on #140 sieve of size 106 μm) and kaolinite clay (4.5−6.0 μm; Wilkinson Kaolin Associates, Gordon, GA) was used in Tests 3 and 4; kaolinite was mixed with a precalculated amount of water to form a slurry that was homogeneously mixed with Ottawa 80/140 sand to have a target initial water saturation. This mixture was packed at an initial porosity $n = 0.35$ with an initial water content $S_w = 0.5$ for Test 3, and $S_w = 0.65$ for Test 4 (Table 1).

2.2. Test Procedure. All tests involved four main stages: (1) specimen preparation, (2) hydrate formation, (3) water injection and drainage, and (4) hydrate dissociation.

Specimen Preparation. The effective stress cell was initially filled with the selected sediment while sensors were placed at the preselected locations. In all tests, the sediment was densified by rodding (successive invasion with a rod of 2.5 cm diameter) on every layer (∼5 cm) to attain the desired porosity, barely invading the previously rodded lower layer

Table 1. Summary of Test Conditions and Procedures

	Measurements	Soil type /Initial conditions	Procedure
Test 1	Pressure (1) Temperature (4) S-wave (2 pairs)	Ottawa 20/30 sand Porosity n=0.4 σ_v'=self weight	Prepare the dry sand specimen in the effective stress cell. Inject water through bottom port to form a ∼6cm high water table. Place the soil chamber inside the SPS. Pressurize the SPS and lower T*. Inject and drain water. Inject water again to saturate the sediment. Turn off cooling system and depressurize the SPS by opening valve 1 (Fig 1).
Test 2	Pressure (2) Temperature (4) S-wave (2 pairs) Surface settlement	Ottawa 20/30 sand Porosity n=0.4 σ_v'=100kPa	
Test 3	Pressure (2) Temperature (6) S-wave (3 pairs) Surface settlement	95% Ottawa 80/140 sand + 5% Kaolinite Porosity n=0.35 Initial water sat. S_w=0.5 σ_v'=100kPa	Prepare the mixed soil specimen in the effective stress cell. Inject water through bottom port to form a 6cm high water table. Place the soil chamber inside the SPS. Pressurize the SPS and lower T*. First water injection and drainage cycle. Second water injection and drainage cycle. Third water injection and drainage cycle. Turn off cooling system and depressurize the SPS by opening valve 1 (Fig 1).
Test 4	Pressure (2) Temperature (6) S-wave (3 pairs) Surface settlement	95% Ottawa 80/140 sand + 5% Kaolinite Porosity n=0.35 Initial water sat. S_w=0.65 σ_v'=100kPa	Prepare mixed specimen in the effective stress cell. Inject water through bottom port to form a 6cm high water table. Place the soil chamber inside the SPS. Pressurize the SPS and lower T*. First water injection and drainage cycle. Second injection using salt water. Turn off cooling system and drainage and depressurization through the bottom port by opening valve 2 (Fig 1).

[a] Operating environmental conditions are P = ∼3.4 MPa, T = 4−6 °C.

dx.doi.org/10.1021/ef101651b |*Energy Fuels* 2012, 26, 480–487

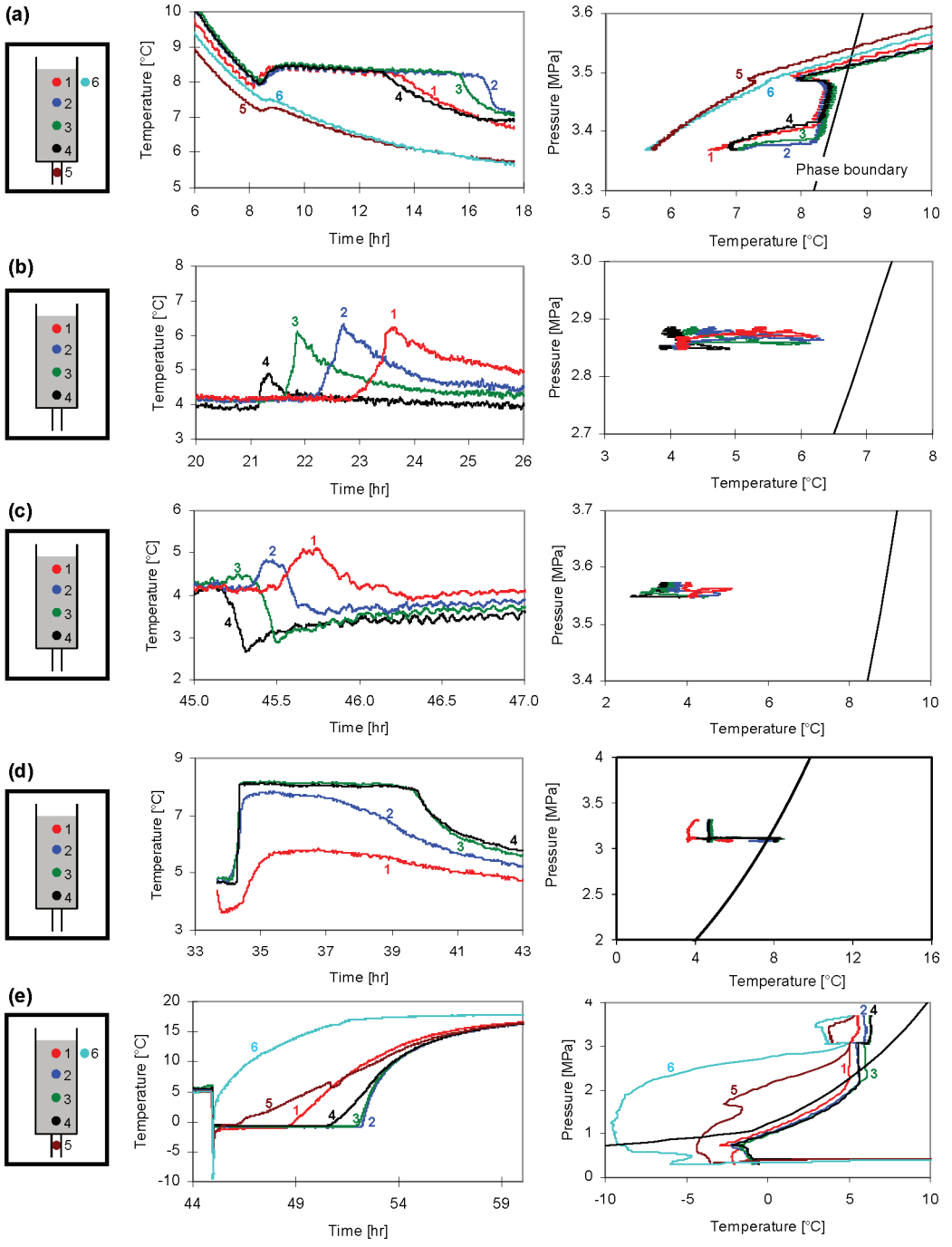

Figure 2. Pressure and temperature histories. Selected test segments during hydrate formation, dissolution, and dissociation. (a) Spontaneous hydrate formation in a gas-filled sand−clay mixture with initial water saturation S_w = 0.5 (Test 3). (b) Hydrate formation in an initially dry, gas-filled sand triggered by water injection (Test 2). (c) Hydrate formation and dissolution during deaired-water injection in gas-filled sand that had some initial hydrate saturation (Test 2). (d) Hydrate formation in an initially water-saturated sand triggered by water drainage and gas invasion (Test 1). (e) Hydrate dissociation by depressurization (final stage in Test 3).

(refer to ASTM D4767[22] for triaxial test); rodding was carefully implemented near sensors to prevent damage. Table 1 summarizes sediment conditions in each of the tests. The vertical effective stress was applied using the spring-based loading system. Finally, the chamber was mounted inside the SPS where all fluid and electrical ports were connected. In all four tests, a volume of water was injected through the bottom port to fill the pore space up to 6 cm from the bottom before pressurization, to prevent hydrate formation near the bottom port and tubing (Note: a capillary rise of ∼58 mm in the clean sand was determined in a preliminary test using a transparent cell).

Hydrate Formation. The SPS was pressurized with CO_2 at room temperature; then the temperature was decreased to 4−6 °C (in all experiments), and kept at constant pressure−temperature conditions inside the CO_2 hydrate stability field overnight (P = ∼3.4 MPa and T = 4−6 °C).

Water Injection and Drainage. After pressurization, deionized and degassed water with no dissolved CO_2 was injected into the gas-rich

dx.doi.org/10.1021/ef101651b |*Energy Fuels* 2012, 26, 480–487

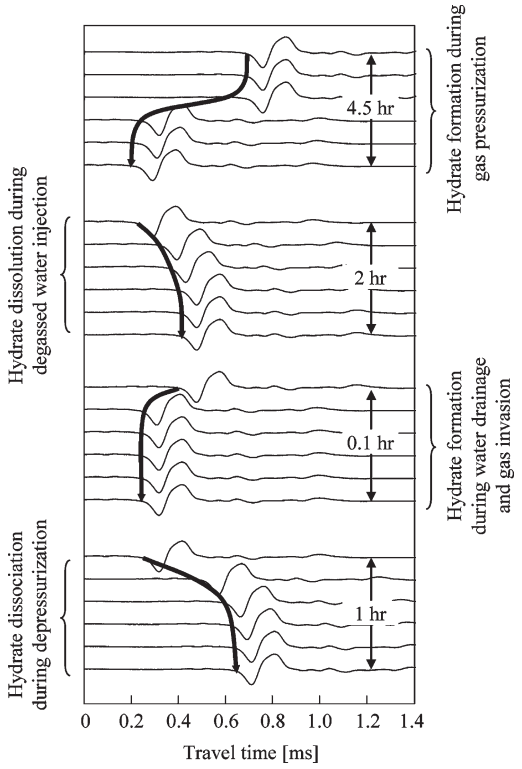

Figure 3. S-wave signatures captured during hydrate formation, dissolution, and dissociation (Test 3).

sediment at an injection rate of 8 mL/min through the port in the bottom plate until the sediment became water-filled. During injection, the instantaneous elevation of the water table was estimated based on the known porosity and the injected volume. During drainage, the water was quickly drained through the same port used for injection (drainage rate from 86 to 116 mL/min) using the pressure inside the SPS to drive fluid flow. The various injection and drainage cycles imposed in the different tests are summarized in Table 1.

Hydrate Dissociation. First, the cooling system was turned off. Hydrate was then dissociated by depressurization. The SPS pressure was first lowered to a value near the hydrate phase transformation boundary. Then, depressurization continued either through the SPS pressure port so that the sediment lost pressure from the top plate (Tests 1, 2, and 4), or through the bottom fluid port in the internal chamber (Test 4). The slower depressurization Tests 1 and 2 prevented ice formation. Faster depressurization rates in Tests 3 and 4 were imposed to promote fines migration; ice formed as a result.

3. EXPERIMENTAL RESULTS

Pressure−temperature histories and corresponding changes in S-wave velocity during hydrate formation, growth, water injection, drainage, and dissociation were obtained during the tests. Selected test segments are reviewed next.

3.1. Initial Hydrate Formation. There was no evidence of hydrate formation ($P-T$ changes were within noise-level) in the dry sediment with low water levels in Tests 1 and 2 during the first ~14 h within stability $P-T$ conditions. However, the partially water saturated sediment in Tests 3 and 4 started to form hydrate after approximately 1 h within the $P-T$ conditions for CO_2 hydrate stability (see pressure decrease and temperature increase during hydrate formation in Figure 2a). Hydrate formation was accompanied by an increase in S-wave velocity and temperature, and a decrease in pressure. The internal thermocouples show that the reaction affected the sediment temperature for more than ~8 h, particularly at the center of the specimen (Figure 2a). In all cases, hydrate formation and gas consumption were estimated from the measured pressure change using the Peng−Robinson equation.

3.2. Water Injection in a Gas-Filled, Hydrate-Free Sediment. The first gas-free water injection caused hydrate formation in the sediment without fines, as indicated by the temperature increase (Test 2, Figure 2b). The initial water injection lasted 3.5 h and the water front moved up at a rate of 76 mm/h, in agreement with the timing of temperature peaks. The S-wave velocity increased where hydrate formed (Figure 3).

3.3. Water Injection in a Hydrate-Bearing Sediment. Following a drainage step, a second injection of gas-free water was imposed into the hydrate-bearing clean sand (Test 2, second injection). Hydrate dissolved near the entry port and the temperature decreased (Figure 2c, thermocouple 4). On the other hand, additional hydrate formed in shallower layers. In general, the S-wave velocity increased when hydrate formed and decreased when hydrate dissolved (Figure 3).

3.4. Water Drainage and Gas Invasion. Hydrate formed when water drainage was allowed (Figure 2d) and the invading gas phase reacted with the residual free water left behind. Water was drained in 20 min while the reaction continued for about ~6 h (Figure 2d). The volume of water drained relative to the volume of injected water is 46% for Test 1, 69% for Test 2, 28% for Test 3, and 25% for Test 4. In Tests 3 and 4, hydrate already had formed before water drainage. Fines also held water; therefore, less water drained out of these specimens.

3.5. Hydrate Dissociation. The cooling system was turned off before the initiation of depressurization. However, the sediment temperature decreased during fast depressurization from an initial pressure near the CO_2−hydrate phase boundary. Cooling results from both depressurization via the Joule−Thomson effect (see Figure 2e thermocouple 6) and hydrate dissociation (other thermocouples in Figure 2e, Test 3). Ice formation started below 0 °C after a supercooling transient. Ice formation and subsequent melting kept the temperature near 0 °C for hours. Finally, the temperature returned asymptotically to the boundary condition ~15 °C. S-wave velocity decreased during hydrate dissociation (Figure 3).

4. GENERAL ANALYSES ON HYDRATE FORMATION, DISSOLUTION, AND DISSOCIATION

Whereas we used CO_2 hydrate for safety restrictions, we note that CO_2 gas forms structure I hydrate which is the same structure as methane hydrate. CO_2 hydrate has also similar heat of formation/dissociation with CH_4 hydrate. The solubility of CO_2 in water is ten times higher than methane solubility in water; high CO_2 solubility facilitates hydrate formation and dissociation studies, and the observation of dissolution effects.

4.1. Fluid Flow and Hydrate Formation. A water−gas mixture may remain inside the thermodynamic hydrate-stability field without forming hydrate for a long time under quiescent conditions. Conversely, hydrate formation is observed if the sediment is subjected to a triggering mechanism such as agitation, mechanical shock, and shear (see Mullin[23] for a general review of crystallization). Results in Figure 2 clearly show that water flow, gas invasion, and increased interfacial area between water and gas can trigger and/or facilitate hydrate formation as well (note that water was in contact with CO_2 before drainage started).

4.2. Hydrate Dissolution. The injection of CO_2-free water in hydrate-bearing sediments induced hydrate dissolution, as indicated by the temperature drop near the injection port in Figure 2d (trace 4; studies on CH_4 and CO_2 hydrate dissolution

dx.doi.org/10.1021/ef101651b |*Energy Fuels* 2012, 26, 480–487

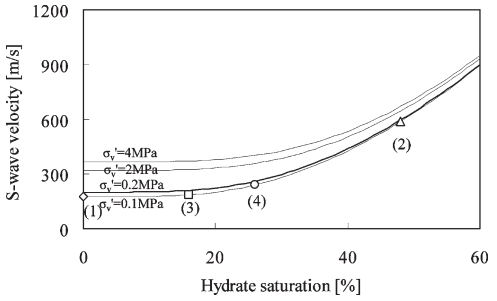

Figure 4. Shear wave velocity in hydrate-bearing sediments. Trends shown are for sands (eq 4). Experimental results correspond to Test 3: (1) ◊ No hydrate, before hydrate formation or after hydrate dissociation. (2) Δ After initial hydrate formation. (3) □ Drop due to hydrate dissolution after gas-free water injection. (4) ○ Hydrate regrowth after water drainage and gas invasion.

in the ocean are reported in ref 24). The amount of hydrate that will dissolve in a pore volume of gas-free water can be estimated from the mass balance of CO_2 in the system as a function of water density ρ_{water} = 1 g/cm^3, hydrate density ρ_{hyd}, gas solubility in water C^{w}_{gas} (mol/kg), gas molar concentration in hydrate C^{hyd}_{gas} [mol/kg], and the water saturation S_w. The change in hydrate saturation ΔS_h for each pore volume of gas-free water that is replaced during injection is

$$\Delta S_h = \frac{C^{w}_{gas}}{C^{hyd}_{gas}} \frac{\rho_w}{\rho_{hyd}} S_w \text{ per pore volume} \quad (1)$$

The amount of water from hydrate dissolution is assumed small compared to the pore volume in this calculation. For CO_2 hydrate, ρ_{hyd} = ~1.11 g/cm^3, $C^{w}_{CO_2}$ = 0.89 mol/kg, $C^{hyd}_{CO_2}$ = 6.58 mol/kg at P = 3 MPa and T = 273 K[25] and eq 1 becomes

$$\Delta S_h \approx 0.12\, S_w \text{ for } CO_2 \text{ hydrate} \quad (2)$$

For CH_4 hydrate, ρ_{hyd} = ~0.94 g/cm^3, $C^{w}_{CH_4}$ = 0.06 mol/kg, $C^{hyd}_{CH_4}$ = 8.20 mol/kg at P = 3 MPa and T = 273nK,[25] hence, the change in hydrate saturation is

$$\Delta S_h \approx 0.008\, S_w \text{ for } CH_4 \text{ hydrate} \quad (3)$$

The computed values are per pore volume of injected gas-free water. In our experiment, and probably in the field, many pore volumes of water are replaced near the water injection port where hydrates experience the most pronounced dissolution.

4.3. Shear-Wave Velocity. The shear-wave velocity of hydrate-free sediment is determined by the effective stresses in the direction of wave propagation $\sigma_{\parallel}'$ and particle motion $\sigma_{\perp}'$. Once hydrate grows in the sediment, the shear wave velocity of hydrate-bearing sediments V_{s_hbs} increases with hydrate saturation S_{hyd},[26]

$$V^2_{s\_hbs} = \alpha \left(\frac{\sigma_{\parallel}' + \sigma_{\perp}'}{2\ \text{kPa}} \right)^{\beta} + \left(\frac{V_h S_h^2}{n} \right)^2 \theta \quad (4)$$

where V_h is the shear-wave velocity of pure hydrate, the factor θ captures the hydrate pore-habit (e.g., cementing or pore filling), and parameters α (shear-wave velocity at 1 kPa mean stress) and β (sensitivity of velocity to the state of stress) are extracted from tests conducted on sediments without hydrate. This expression can be used to analyze geophysical data, such as the time series measured during Test 3, shown in Figure 3.

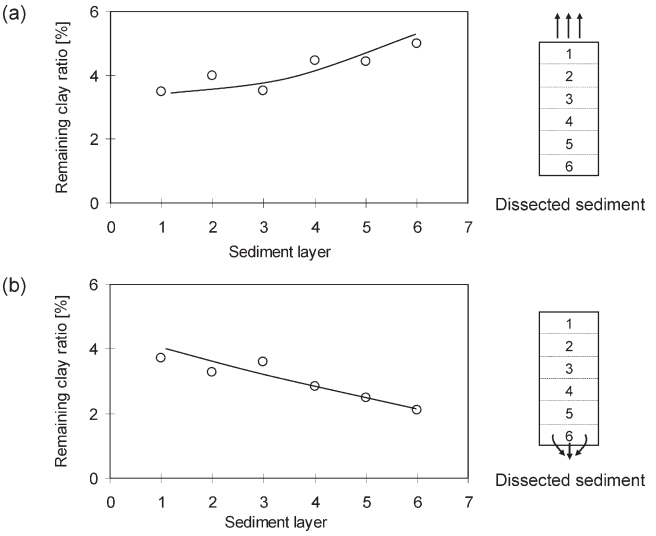

Figure 5. Fines migration during hydrate dissociation. Resulting fines distribution: (a) after upward flow (Test 3), and (b) after drainage through the bottom port (Test 4).

Figure 4 shows the variation of S-wave velocity versus hydrate saturation, for different effective stress levels. The parameters α = 80 m/s and β = 0.25 are measured for the hydrate-free sand, V_h = 1964 m/s is obtained from the literature,[27] and θ = 0.25 is inferred from the S-wave velocity V_s = 588 m/s measured at S_h = 48% in Test 3 (hydrate saturation based both on pressure drop and on initial water saturation. Note: the value of θ can range between 0.08 and 0.25, according to Santamarina and Ruppel[26]). Using this plot, one can estimate the evolution in hydrate saturation during experiments from the measured S-wave velocities. For example, consider Test 3: if the hydrate saturation after initial hydrate formation was S_h = 48%, dissolution near the entry port caused a drop in hydrate saturation to S_h = 16%, and hydrate regrew after drainage and gas invasion to reach S_h = 27% (Figure 4).

It follows from this discussion that the parameters of the semi-empirical eq 4 can be determined for a given sediment knowing the stiffness response to stress in the hydrate free sediment (α and β), and the stiffness evolution with hydrate saturation (θ).

5. ANALYSES: THE ROLE OF FINES

Fines migration and clogging depend on geometric constraints, i.e., the relative size of the migratory fines with respect to the pore throat size in the host sediment skeleton. A single particle with diameter d can migrate through a packing of grains size D when $D/d > 2.4$ for simple cubic packing to $D/d > 6.4$ for cubic tetrahedral packing.[1,28] When many migrating particles reach a pore throat at once, 3−5 migrating particles can form a bridge; therefore, clogging can occur when migrating fines are D/d = 12−30 times smaller than the sediment grains.[3,29,30]

The average particle diameter D of Ottawa 80/140 sand is ~0.105 mm and the particle diameter d of kaolinite is 4.5−6.0 μm. Given that D/d ~20, single kaolin particles can migrate through the sand skeleton; however, a high concentration of kaolinite particles could clog pore throats by forming bridges. Evidence for these two cases is presented next.

5.1. Fines Migration. Specimens were dissected into six layers (the thickness of each layer was ~5 cm) at the end of Tests 3 and

dx.doi.org/10.1021/ef101651b |Energy Fuels 2012, 26, 480–487

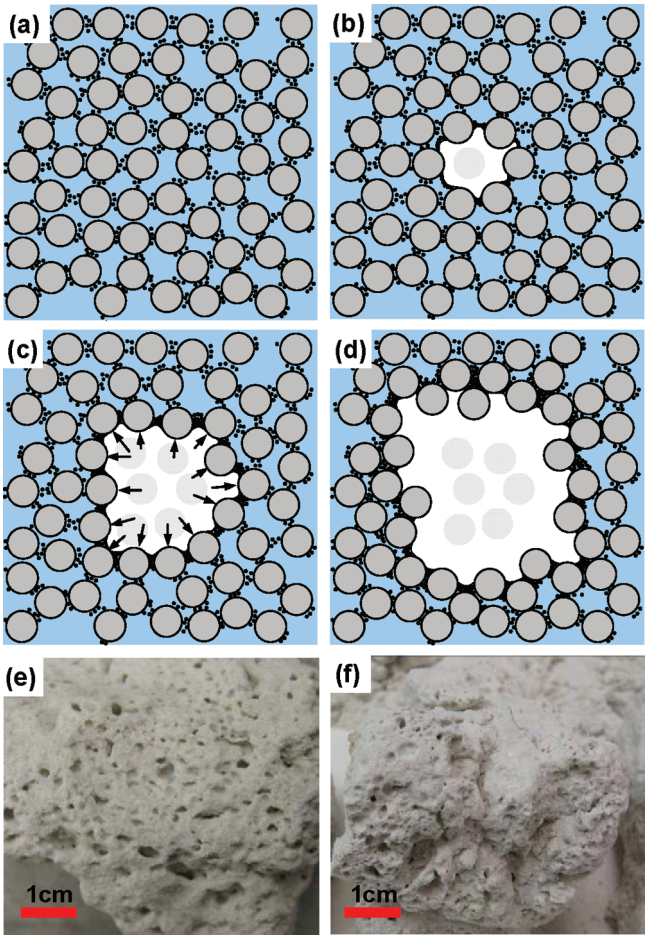

Figure 6. Vuggy structure formation due to local clogging and particle displacement during gas bubble expansion (Test 3). (a) Distributed fines in a water-saturated sediment. (b) Gas bubble nucleation during hydrate dissociation: fines move with the gas−water interface as the gas bubble grows. (c) High fines concentration clogs pore throats. (d) Further gas bubble growth can push sand particles away. (e and f) Observed vuggy structure in Ottawa sand with 5% fines content.

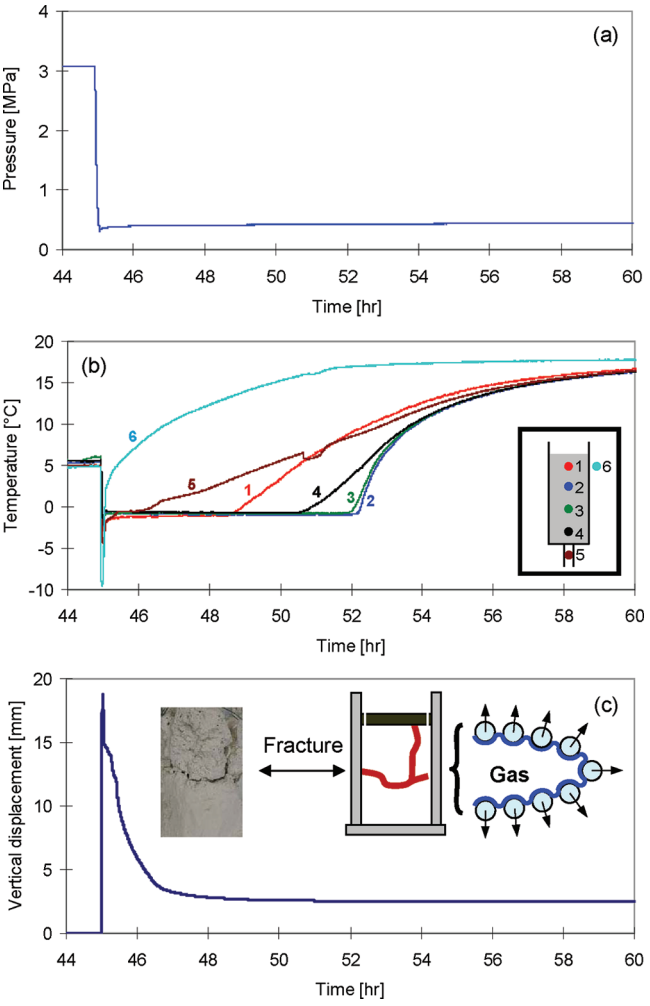

Figure 7. Gas-driven fracture formation (Text 3). (a) Hydrate dissociation by SPS depressurization (i.e., decrease in the boundary total stress). (b) Rapid depressurization induces ice formation concurrent with hydrate dissociation. (c) Gas expansion creates gas-driven fracture formation that facilitates gas evacuation.

4 and clay content was measured for each layer using sieve analyses. Results in Figure 5 show that fines migrated toward the top of the sediment column when depressurization occurred through the top plate (Test 3, Figure 5a), and toward the lower part of the sediment column when depressurization occurred through the bottom port of the chamber (Test 4, Figure 5b). These data confirm that small particles migrated during gas production.

5.2. Clogging and Vuggy Structure Formation. Kaolinite may clog Ottawa 80/140 where high particle concentrations develop. Let us consider a growing gas bubble in water-saturated sandy sediment with clay fines (Figure 6). The fine particles that are not part of the load-carrying granular skeleton can move along with the interface of the expanding bubble surface due to surface charge[31] and capillary effects. The bubble can grow without displacing the skeletal sand particles when the fines content on the bubble surface is low (Figure 6b). If the mass of fines per unit surface area of the bubble is high enough to form bridges and clog pore throats in the sand, then the expanding gas bubble will locally push away the skeletal sand particles as long as the pressure of the gas bubble can create a sufficiently high force against the bounding sand grains (Figure 6c). The vuggy, sponge-like structure observed after depressurization in Test 3 (Figure 6d and pictures in Figures 6e and 6f) confirms the effect of clogging in this hypothetical sequence of events (note that we did not observe the vuggy structure in other Tests 1, 2, and 4.

5.3. Gas-Driven Fractures. Continued gas expansion can lead to the development of gas-driven fractures when the gas pressure exceeds the total stress; fractures are observed in Figure 7c (Test 3). Hydrate dissociation under undrained, constant-volume conditions (i.e., fast thermal stimulation) can cause the development of substantial pressure: using the modified Peng−Robinson equation, the theoretical pressure could exceed ~2000 MPa (see also Kwon et al.[11]). For a more realistic condition, consider a pore that is initially filled with hydrate: if the water produced by dissociation is allowed to drain but the gas remains trapped by capillarity, then, the gas would build a pressure equal to 14 MPa if the capillary entry pressure at pore throats prevents gas expansion into neighboring pores. Typical depths for gas hydrate stability zones in marine sediments are shallower than 800 m below seafloor, which means a maximum vertical effective stress $\sigma_v' \approx 8$ MPa. If the combined water pressure and

dx.doi.org/10.1021/ef101651b |*Energy Fuels* 2012, 26, 480–487

Table 2. Sediment Characteristics and Physical Properties: The Relevance of Fines and Potential Phenomena during Gas Production

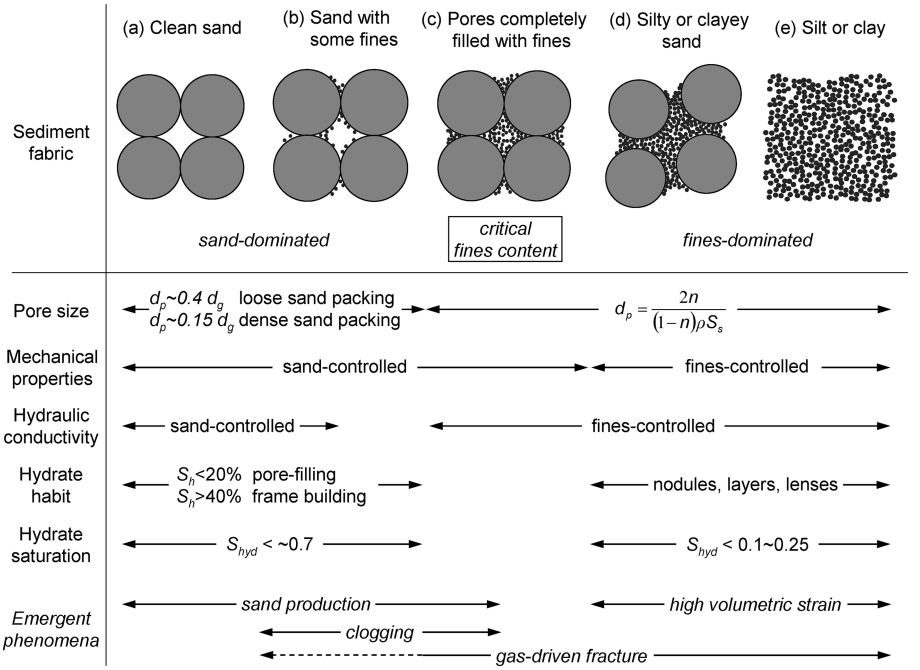

effective stress $P_w + \sigma_v'$ is lower than ~14 MPa, gas-driven fractures will occur even if the water dissipation rate is faster than the hydrate dissociation rate.

If the capillary pressure at the sediment pore throats is smaller than the effective stress, released gas during dissociation will expand without causing grain displacement. However, a small fraction of fine particles can migrate and induce clogging which increases the capillary pressure dramatically. In other words, the probability of gas-driven fracture formation will increase if fines are present in otherwise sandy sediments.

5.4. Role of Fines: Summary. The existence of fines in sediments can dramatically change the sediment properties. Let us assume a sediment made of clean sands (Table 2, column a). As the fines content increases, fines start filling voids (Table 2, column b). Let us define the "critical fines content" FC* as the ratio of the weight of fines w_f to the weight of coarse grains w_c when the voids between coarse grains are fully filled with fines (Table 2, column c). Gravimetric-volumetric analyses show that the critical fines content can be expressed as a function of the void ratio of the coarse e_c and fine grain e_f packings:

$$FC^* = \frac{w_f}{w_c} = \frac{e_c}{1 + e_f} \approx \frac{e_c}{1 + e_f^{1kPa}} \quad (5)$$

The critical fines content FC* is 35% for silt (e_f = 0.7), 24% for kaolinite (e_f = 1.47), 12% for Illite (e_f = 3.7), and 9% for montmorillonite (e_f = 5.4) when the void ratio of the sand is assumed at e_c = 0.6. In other words, the critical fines content decreases as the plasticity of fines increases.

Mechanical properties such as stiffness and strength are controlled by the sand skeleton as long as sand grains contact each other, FC < FC* (Table 2, columns a–c). Once sand particles are separated, FC > FC*, fines start forming the continuous load-carrying skeleton and control the mechanical properties of sediments (Table 2, columns d and e).

Phenomena that take place in pores, such as fluid flow and hydrate formation/dissociation, respond to pore size (Table 2). Pore size d_p in clean sands with grain diameter d_g ranges from $d_p = 0.4d_g$ for loose packing to $d_p = 0.15d_g$ for dense packing. In case of 100% fine sediments, pore size can be estimated as a function of the sediment porosity n, the mineral density ρ_m, and the specific surface of fines S_S as $d_p = 2n/[(1 - n)\rho_m S_s]$.[32]

Clearly, even small fraction of fines can decrease pore size and the sediment permeability dramatically. In particular, the sediment permeability is that of the sand when FC ≪ FC*, however, it decreases to the permeability of the clay when the fines content approaches the critical fines content FC*.

Hydrate saturation and pore habit change with fines content too. In coarse sediments in the Nankai Trough and Gulf of Mexico, pore-filling hydrate saturation can exceed 70%. However, low hydrate saturation prevails in fine-grained sediments and it is typically found in the form of lenses and nodules.[33−35]

The potential consequences of fines during gas production from hydrate-bearing sediments include gradual clogging, decreased permeability, and gas-driven fractures in sandy sediments (Table 2). Hydrate dissociation in clayey sediments will be accompanied by excess gas pressure generation and gas-driven fractures.

6. CONCLUSIONS

The advection of gas-free water into hydrate-bearing sediments dissolves hydrate. The change in hydrate saturation "ΔS_h for each pore volume of replaced water" is $\Delta S_h \approx 0.12 S_w$ in CO_2 hydrate and $\Delta S_h \approx 0.008 S_w$ in CH_4 hydrate, where S_w is the initial water saturation.

The shear-wave velocity reflects the sediment stress−hydrate condition. The S-wave velocity can be captured using a Hertzian-type

dx.doi.org/10.1021/ef101651b |Energy Fuels 2012, 26, 480–487

semiempirical relationship that accounts for effective stress, hydrate saturation, and pore habit. When properly calibrated, this equation can be used to monitor changes in hydrate saturation.

A sandy sediment has a critical content of fines FC* when fine clayey grains fill pores between sand grains. The critical fines content decreases with clay plasticity, and can be FC* < 10% for montmorillonite. Fine grains govern all sediment properties when the fines content approaches and exceeds FC*.

Field data show that the in situ hydrate saturation and hydrate pore habit are affected by fines content: pore-filling hydrate saturation can exceed S_h ~70% in clean sands, while hydrate saturation in clayey sediments tends to be low, S_h < 30%, and distributed in the form of nodules and lenses.

The migration of fine particles that are not part of the load-carrying granular skeleton depends on geometric constraints such as the relative size of the migratory fines with respect to the size of pore throats in the sediment. When geometric conditions are satisfied, gas production in hydrate-bearing sediments containing fines can induce fines migration, local accumulation and clogging, the formation of a vuggy structure, and gas-driven fracture formation.

Even a small fraction of fines can dramatically reduce the permeability of a sandy sediment. Thus, the presence of fines in otherwise clean sands will hinder gas recovery.

AUTHOR INFORMATION

Corresponding Author

*E-mail: kocee76@hotmail.com; phone: 404-643-6261.

ACKNOWLEDGMENT

Support for this research was provided by the U.S. Department of Energy through The National Methane Hydrate R&D Program. Additional funding was provided by the Goizueta Foundation. We are grateful to Connor Barrett for editing the manuscript and J. Alford for helping during the experiments. The Oak Ridge National Laboratory Methane Hydrates project is sponsored by the U.S. DOE, Office of Fossil Energy under FWP FEAB111. Oak Ridge National Laboratory is managed by UT-Battelle, LLC, for the U.S. Department of Energy under contract DE-AC05-00OR22725.

REFERENCES

(1) McDowell-Boyer, L. M.; Hunt, J. R.; Sitar, N. *Water Resour. Res.* **1986**, *22* (13), 1901–1921.

(2) Kampel, G.; Goldsztein, G. H.; Santamarina, J. C. *Applied Phys. Lett.* **2008**, *92*, 084101:1–3.

(3) Valdes, J. R.; Santamarina, J. C. *Can. Geotech. J.* **2008**, *45*, 177–184.

(4) Papamichos, E.; Vardoulakis, I.; Tronvoll, J.; Skjærstein, A. *Int. J. Numer. Anal. Methods Geomech.* **2001**, *25*, 789–808.

(5) Hardin, B. O. *Journal of Geotech. Geoenviron. Eng.* **1985**, *111* (10), 1177–1192.

(6) Cheng, Y. P.; Nakata, Y.; Bolton, M. D. *Geotechnique* **2003**, *53* (7), 633–641.

(7) Guimaraes, M. S.; Valdes, J. R.; Palomino, A. M.; Santamarina, J. C. *Int. J. Miner. Process.* **2007**, *81*, 237–247.

(8) Shin, H.; Santamarina, J. C. *Earth Planet. Sci. Lett.* **2010**, *299*, 180–189.

(9) Rutqvist, J.; Moridis, G. J.; Grover, T.; Collett, T. *J. Pet. Sci. Eng.* **2009**, *67*, 1–12, DOI: 10.1016/j.petro.2009.02.013.

(10) Wilder, J. W.; Moridis, G. J.; Wilson, S. J.; Kurihara, M.; White, M. D.; Masuda, Y.; Anderson, B. J.; Collett, T. S.; Hunter, R. B.; Narita, H.; Pooladi-Darvish, M.; Rose, K.; Boswell, R. *6th International Conference on Gas Hydrate*, July 6−10, 2008, Vancouver, Canada.

(11) Kwon, T. H.; Cho, G. C.; Santamarina, J. C. *Geochem. Geophys. Geosyst.* **2008**, *9*, Q03019.

(12) Garg, S.; J., P.; Katoh, A.; Baba, K.; Fujii, T. *J. Geophys. Res.* **2008**, *113*, B01201.

(13) Moridis, G. J.; Sloan, E. D. *Energy Convers. Manage.* **2007**, *48* (6), 1834–1849.

(14) Ahmadi, G.; Ji, C.; Smith, D. H. *Journal of Pet. Sci. Eng.* **2004**, *41* (4), 269–285.

(15) Kawamura, T.; Ohtake, M.; Sakamoto, Y.; Yamamoto, Y.; Haneda, H.; Komai, T.; Higuchi, S. *International Offshore and Polar Engineering Conference*, June 21−26, 2009, Osaka, Japan,

(16) Tang, L. G.; Xiao, R.; Huang, C.; Feng, Z. P.; Fan, S. S. *Energy Fuels* **2005**, *19*, 2402–2407.

(17) Linga, P.; Haligva, C.; Nam, S. C.; Ripmeester, J. A.; Englezon, P. *Energy Fuels* **2009**, *23*, 5508–5516.

(18) Linga, P.; Haligva, C.; Nam, S. C.; RIpmeester, J. A.; Englezos, P. *Energy Fuels* **2009**, *23*, 5496–5507.

(19) Kono., H. O.; Narasimhan, S.; Song, F.; Smith, D. H. *Power Technol.* **2002**, *122*, 239–246.

(20) Oyama, H.; Konno, Y.; Masuda, Y.; Narita, H. *Energy Fuels* **2009**, *23*, 4995–5002.

(21) Phelps, T. J.; Peters, D. J.; Marshall, S. L.; West, O. R.; Liang, L.; Blencoe, J. G.; Alexiades, V.; Jacobs, G. K.; Naney, M. T.; Heck, J. L., Jr. *Rev. Sci. Instrum.* **2001**, *72* (2), 1514–1521.

(22) ASTM D4767-04. Standard test method for consolidated undrained triaxial compression test for cohesive soils, 2004.

(23) Mullin, J. W. *Crystallization*: Butterworth-Heinemann: London, 2001.

(24) Rehder, G.; Kirby, S. H.; Durham, W. B.; Stern, L. A.; Peltzer, E. T.; Pinkston, J.; Brewer, P. G. *Geochim. Cosmochim. Acta* **2004**, *68* (2), 285–292.

(25) Jung, J. W.; Espinoza, D. N.; Santamarina, J. C. *J. Geophys. Res.* **2010**, *115*, B10102.

(26) Santamarina, J. C.; Ruppel, C. *6th International Conference on Gas Hydrate*, July 6−10, 2008, Vancouver, Canada.

(27) Sloan, E. D.; Koh, C. H. *Clathrate Hydrates of Natural Gases*, 3rd ed.; Taylor & Francis Group, 2008.

(28) Kenny, T. C.; Chahal, R.; Chiu, E.; Ofoegbu, G. I.; Omange, N.; Ume, C. A. *Can. Geotech. J.* **1985**, *22* (1), 32–43.

(29) Ramachandran, V.; Fogler, H. S. *J. Fluid Mech.* **1999**, *385*, 129–156.

(30) Watson, P. D. J.; John, N. W. M. *Geotextiles Geomembranes* **1999**, *17*, 265–280.

(31) Wan, J.; Tokunaga, T. K. *J. Colloid Interface Sci.* **2002**, *247*, 54–61.

(32) Phadnis, H. S.; Santamarina, J. C. *Geotech. Lett.* **2011**No. 10.1680/geolett.11.00008.

(33) Uchida, T.; Lu, H.; Tomaru, H. The MITI Nankai Trough shipboard scientists. *Resour. Geol.* **2004**, *54* (1), 35–44.

(34) Boswell, R.; Shelander, D.; Lee, M.; Latham, T.; Collett, T.; Guerin, G.; Moridis, G.; Reagan, M.; Goldberg, D. *Mar. Pet. Geol.* **2009**, *26* (8), 1499–1512.

(35) Tréhu, A. M.; Long, P. E.; Torres, M. E.; Bohrmann, G.; Rack, F. R.; Collett, T. S.; Goldberg, D. S.; Milkov, A. V.; Riedel, M.; Schultheiss, P.; Bangs, N. L.; Barr, S. R.; Borowski, W. S.; Claypool, G. E.; Delwiche, M. E.; Dickens, G. R.; Gracia, E.; Guerin, G.; Holland, M.; Johnson, J. E.; Lee, Y.-J.; Liu, C.-S.; Su, X.; Teichert, B.; Tomaru, H.; Vanneste, M.; Watanabe, M.; Weinberger, J. L. *Earth Planet. Sci. Lett.* **2004**, *222*, 845–862.